Journal of Applied Fluid Mechanics, Vol. 18, No. 4, pp. 835-849, 2025.
Available online at www.jafmonline.net, ISSN 1735-3572, EISSN 1735-3645.
https://doi.org/10.47176/jafm.18.4.3005

Flow-induced Flutter Derivatives of Bridge Decks

B. Su[1], Y. Liu[1], M. Chambalile[1], G. Wang[1], M. M. Alam[2,†] and E. Barati[3]

[1] *Faculty of Civil Engineering and Mechanics, Jiangsu University, Zhenjiang 212000, China*
[2] *Center for Turbulence Control, Mechanical and Automation Engineering Department, Harbin Institute of Technology (Shenzhen), Shenzhen, 518055, China*
[3] *Department of Mechanical Engineering, Khayyam University, Mashhad, Iran*

†Corresponding Author Email: alam@hit.edu.cn

ABSTRACT

This paper presents two-dimensional numerical simulations of the self-excited forces on two bridge decks: a streamlined one (Great Belt Bridge) and a bluff one (Sunshine Skyway Bridge). It employs forced vibration simulations using the Open-source code OpenFOAM for flutter derivative identifications. A wide sensitivity study is conducted on the effects of turbulence model, Reynolds number, vibration amplitude, and wind attack angle on flutter derivative identifications. The key findings are as follows. (i) k-ε model shows its superiority in simulating self-excited forces on a bluff bridge deck, while SST k-ω exhibits advantages in the case of a streamlined bridge deck. (ii) Compared with a streamlined bridge deck, flutter derivatives of a bluff bridge deck are more sensitive to the Reynolds number due to the generation of more vortices resulting from flow separation. Both the generation and convection of the vortices are largely affected by the Reynolds number. (iii) Flutter derivatives of the bridge decks can be considered as constants if the vertical amplitude ratio and torsional amplitude are lower than 0.025 and 2°, respectively. Increasing vibration amplitude may result in remarkable variations of some flutter derivatives. (iv) The angle of attack changes the flutter derivatives by affecting the wind pressure distribution on the bridge surface. Its impact on a bluff bridge deck is larger than on a streamlined bridge deck. Besides presenting a detailed study of identifying flutter derivatives using OpenFOAM, this research provides valuable references for setting reasonable values of the investigated factors for identifying flutter derivatives of bluff and streamlined bridge decks.

Article History

Received July 27, 2024
Revised October 23, 2024
Accepted November 21, 2024
Available online February 4, 2025

Keywords:

Flutter derivative
Turbulence mode
Amplitude
Angle of attack
Reynolds number

1. INTRODUCTION

Flutter in bridges is a self-excited vibration caused by the interaction of aerodynamic forces and structural vibrations. It occurs when wind speed reaches a critical level, leading to dynamic coupling and increasing vibration amplitudes, potentially resulting in instability or structural failure. Flutter derivatives play a crucial role in aerodynamic stability analysis, helping engineers predict the onset of flutter and assess bridge stability under varying wind conditions. Since the wind-induced failure of the original Tacoma bridge (Amman et al., 1941), extensive research has been carried out on the aerodynamics and aeroelasticity of bridges or bluff bodies (Scanlan, 1993; Bhatt & Alam, 2018; Lin & Alam, 2024). Davenport and Allan (1962) were the first to introduce the concept of aerodynamic admittances to simulate the aerodynamic buffeting force. Later, Scanlan (1993) put forward the concept of flutter derivatives to simulate the self-excited force. Since then, the analytical framework of aerodynamic admittances and flutter derivatives has been largely followed and studied in wind engineering. In the early stage, wind tunnel experiments were the primary method for identifying flutter derivatives and have been extensively utilized by many researchers (Neuhaus et al., 2009; Siedziako et al., 2017; Zhang & Zhang, 2017). However, with the advancements in computer science, computational fluid dynamics (CFD)-based numerical simulations have been employed for flutter derivative identifications (Xu et al., 2016; Xu & Zhang 2017; Bombardieri et al., 2019). This approach has proven to reduce the cost and time required for wind tunnel experiments (Montoya et al., 2018). Aerodynamic buffeting refers to forced vibrations caused by external airflow, such as turbulence or gusts, and is characterized by random and irregular oscillations. While it is generally independent of the structure's natural frequency, it may not lead to structural instability; however, it can impact comfort and durability.

Nomenclature

B	deck width	L	lifting force
C_{L_h}	lift coefficients associated with the vertical bending	M	pitching moment
C_{L_α}	lift coefficients associated with torsional motion	U	mean wind speed
C_{M_h}	pitching moment coefficients associated with vertical bending	α_0	torsional amplitude
C_{M_α}	pitching moment coefficients associated with torsional motion	ω	circular frequency of structural vibration
h_0	vertical bending amplitude	ρ	air density
K	reduced frequency		

Forced- and free-vibration methods are the two common CFD techniques to identify flutter derivatives. In forced vibrations, the deck section is forced to undergo harmonic vibration, and the flutter derivatives are derived from the displacement and self-excited force signals (Cao & Sarkar, 2010). On the other hand, in free vibrations, the deck section is allowed to vibrate freely under the effect of oncoming flow, and the flutter derivatives are determined from the vibration frequency and damping ratio (Brownjohn & Bogunovic, 2001). Unlike free vibrations, forced vibrations exhibit greater stability and reliability within the high reduced wind speed range and is hence largely advanced in recent years.

Although the identifications of flutter derivatives from numerical simulation results are effective (Abbas et al., 2017), the numerical simulations need validation, following grid and time-step independence tests. Indeed, many factors including turbulence model, vibration amplitude, Reynolds number, and wind angle of attack may affect the simulation results. It is thus necessary to systematically evaluate the effects of these factors and provide references for setting reasonable values in flutter derivative identifications. Brusiani et al. (2013) compared k-ε, k-Omega, SST k-ω turbulence models in flutter derivative identifications of Great Belt East bridge and found that SST k-ω model is preferable as the corresponding results are close to some experimental data available in the literature. Patruno (2015) proved that the SST k-ω model is surprisingly accurate in predicting the flutter onset velocity. De Miranda et al. (2015) simulated the flow field of a twin box deck section using both LES and SST k-ω models and found different advantages under different gap ratios. Schewe & Larsen (1998) concluded that slender bodies with sharp-edged cross sections such as bridge box girders may suffer pronounced Reynolds number effects (Alam, 2023; Zhou et al. 2024). Further research by Bruno and Fransos (2008) showed that the flutter derivatives affected by inertial and viscous in-motion forces are more sensitive to the Reynolds number. Zhou and Ma (2010) investigated Reynolds number effects on aerostatic coefficients of Great Belt East Bridge and Sutong Bridge and concluded that the effect cannot be neglected. Noda et al. (2003) found that the flutter derivatives are contingent on vibration amplitudes. The effect of vibration amplitude on flutter derivatives is then highlighted by several researchers (Lin et al., 2019; Zhang et al., 2019, 2020a, b). Conducting experiments in a water tunnel for flutter derivative identification, Starossek et al. (2009) proved that the angle of attack has a significant impact on the critical wind speed. In the study of a long-span suspension bridge, Tang et al. (2018) found that the streamlined steel plate presents the characteristics of a blunt body under high attack angles. Tang et al. (2019) studied the flutter performance of twin-box bridge girders and proved that a large attack angle may drive the bridge to torsional flutter instability at lower wind speeds. From the literature review presented above, it is obvious that the identification of flutter derivatives can be affected by several factors. Although some parametric analyses on the effects of some factors are available (Mannini et al., 2016; Lin et al., 2019; Wu et al., 2020), systematic evaluations of their effects on flutter derivatives of different cross-sections are yet scarce.

Computational Fluid Dynamics (CFD) offers significant advantages over traditional wind tunnel experiments. CFD is generally more cost-effective and allows easy adjustment of model parameters without size limitations, making it suitable for structures of any scale. Additionally, CFD can capture more detailed flow field information, including velocity and pressure fields. Lastly, CFD is better suited for simulating complex flow conditions, such as turbulence and flow separation, providing a more comprehensive and in-depth understanding of fluid dynamics. OpenFOAM is used in bridge simulations to model the interaction between fluid and bridge structures through Computational Fluid Dynamics (CFD) and assess their performance under wind loads. Moreover, OpenFOAM can calculate self-excited forces and perform fluid-structure interaction analysis by integrating with structural analysis software, allowing for a comprehensive evaluation of the bridge's overall response. Therefore, we leveraged the advantages of OpenFOAM to conduct simulation analyses, performing a thorough evaluation of two types of bridge sections.

In order to enhance the reference material for flutter derivative identifications from numerical simulation results, our current study encompasses both streamlined and bluff bridge decks. We investigate the impact of turbulence models, Reynolds numbers, vibration amplitudes, and wind attack angles on flutter derivative identifications utilizing the open-source CFD software—OpenFOAM. This paper is organized as follows. Firstly, we present the fundamental theory of flutter derivative identifications, followed by a description of the OpenFOAM simulation process. Subsequently, we discuss the effects of the four parameters based on the numerical simulation results. Finally, we draw conclusions to offer valuable insights for flutter derivative identification pertaining to similar bridge decks.

2. PROBLEM SETTING

2.1 Fundamental Theory

Considering a two-dimensional bridge deck in a smooth flow, the aerodynamic forces and moments can be expressed in a mixed time-frequency domain as (Scanlan & Tomo, 1971)

$$L = \frac{1}{2}\rho U^2(2B)(KH_1^*\frac{\dot{h}}{U} + KH_2^*\frac{\alpha B}{U} + K^2H_3^*\alpha + K^2H_4^*\frac{h}{B}), \tag{1a}$$

and

$$M = \frac{1}{2}\rho U^2(2B^2)(KA_1^*\frac{\dot{h}}{U} + KA_2^*\frac{\alpha B}{U} + K^2A_3^*\alpha + K^2A_4^*\frac{h}{B}), \tag{1b}$$

where L and M represent lift force and pitching moment, respectively; B is the deck width; ρ is the air density; U is the mean wind speed; ω is the circular frequency of structural vibration; $K = B\omega/U$ is the reduced frequency; H_i^*, A_i^* (i=1、2、3、4) represent flutter derivatives, which are functions of K.

The bridge deck is forced to perform single degree-of-freedom vertical or torsional harmonic vibration as

$$h = h_0 e^{i\omega t}\ , \tag{2a}$$

and

$$\alpha = \alpha_0 e^{i\omega t}\ , \tag{2b}$$

where h_0 is the vertical bending amplitude, and α_0 is the torsional amplitude.

Plugging equations (2a, b) into equations (1a, b), the aeroelastic forces coefficients can be obtained as

$$C_{L_h} = \frac{L}{\frac{1}{2}\rho U^2(2B)} = K_hH_1^*\frac{i\omega h_0 e^{i\omega t}}{U} + K_h^2H_4^*\frac{h_0 e^{i\omega t}}{B}\ , \tag{3a}$$

$$C_{M_h} = \frac{M}{\frac{1}{2}\rho U^2(2B^2)} = K_hA_1^*\frac{i\omega h_0 e^{i\omega t}}{U} + K_h^2A_4^*\frac{h_0 e^{i\omega t}}{B}, \tag{3b}$$

$$C_{L_\alpha} = \frac{L}{\frac{1}{2}\rho U^2(2B)} = K_\alpha H_2^*\frac{Bi\omega\alpha_0 e^{i\omega t}}{U} + K_\alpha^2H_3^*\alpha_0 e^{i\omega t}, \tag{3c}$$

and

$$C_{M_\alpha} = \frac{M}{\frac{1}{2}\rho U^2(2B^2)} = K_\alpha A_2^*\frac{Bi\omega\alpha_0 e^{i\omega t}}{U} + K_\alpha^2A_3^*\alpha_0 e^{i\omega t}, \tag{3d}$$

where C_{L_h} and C_{L_α} are lift coefficients associated with the vertical bending and torsional motion, respectively, while C_{M_h} and C_{M_α} are pitching moment coefficients associated with vertical bending and torsional motions, respectively.

Time histories of the force coefficients and displacement can lead to estimations of the flutter derivatives using the least square method.

2.2 Simulation Strategy

As shown in Fig. 1, two-dimensional models of two typical bridge decks are studied here. Section A is a streamlined section of the Great Belt Bridge in Denmark, and section B is a bluff section simplified from the bridge deck of the American Sunshine Skyway Bridge. Scaled models of 1:10 are used for simulations. The resulting deck width B is 3.1 m for section A and 4.5 m for section B. The geometric model and mesh generation are generated by Salomé, which is a free software distributed under the terms of the GNU Lesser General Public License, providing a generic platform for pre- and post-processing of numerical simulation (Ribes & Caremoli, 2007).

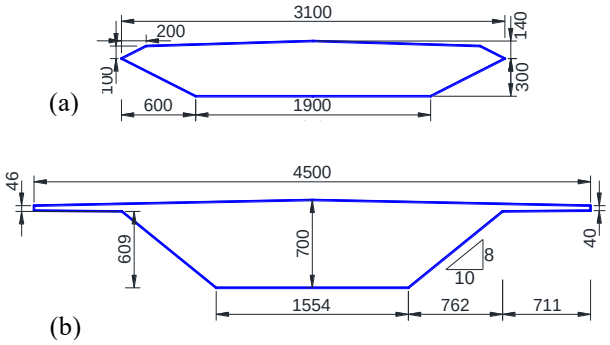

Fig. 1 Two-dimensional bridge deck sections (unit: cm): (a) section A, streamlined shape, and (b) section B, bluff shape

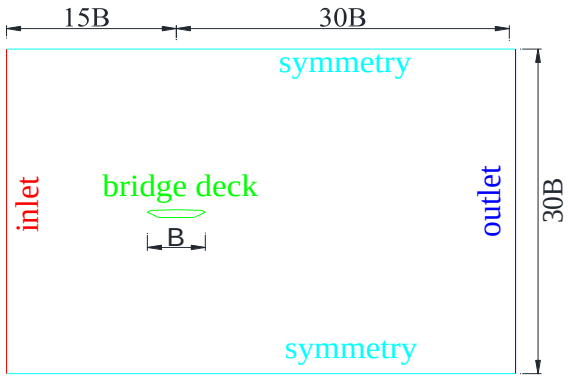

Fig. 2 Schematic diagram for the computational domain and boundary conditions

The computational domain size, following Bruno et al. (2001), is illustrated in Fig. 2. The geometric center of the bridge deck section is 15B from the inlet, 30B from the outlet in the horizontal direction, and 15B from the two symmetry edges. The blockage ratios of sections A and B are respectively 0.47% and 0.52%, which satisfy the requirement (lower than 3%) suggested by Baetke et al. (1990), Zheng and Alam (2017, 2019), and Mondal & Alam (2023). The bridge deck surfaces are considered non-slip walls, and other boundary conditions are shown in Fig. 2.

Unstructured grids are used for the most computing area while structured grids are used near the surfaces of the bridge decks. The number of structured grids for sections A and B are 6930 and 7142, respectively, and the numbers of the unstructured grids are 45761 and 66917, respectively. The mesh for section A is presented in Fig. 3

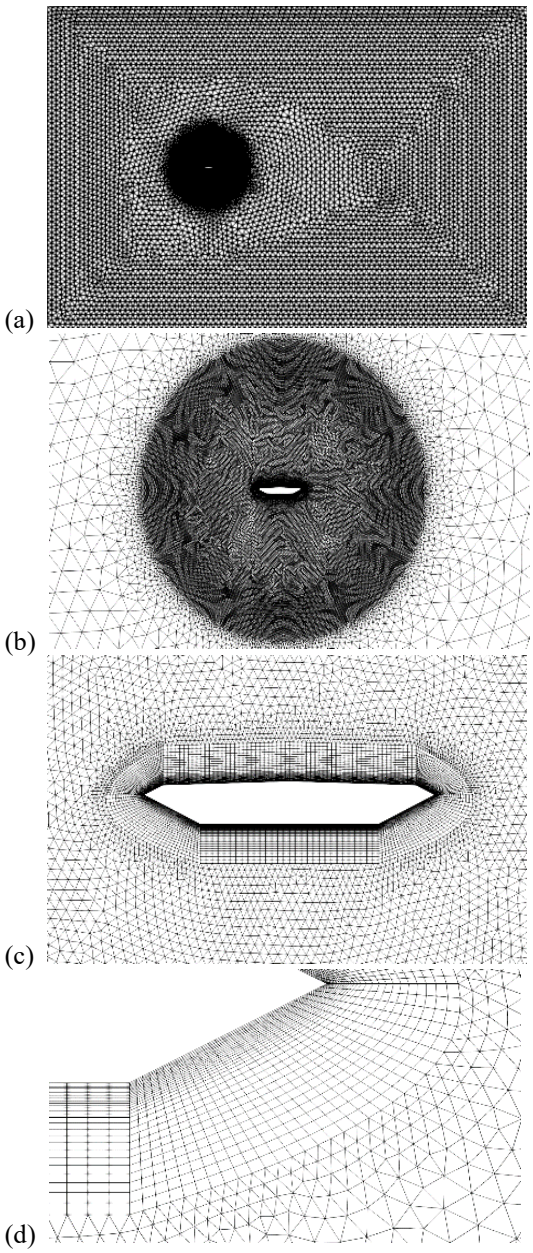

Fig. 3 Hybrid mesh of section A (deck of great belt bridge): (a) computational domain; (b) refined mesh around the deck; (c) mesh near deck; and (d) transition between structured and unstructured grids

as an example. The wall functions of K, ε, ω and μ_t (turbulent viscosity) are selected following different turbulence models in OpenFOAM.

The mesh size is controlled by the first layer of the mesh near the wall. The dimensionless number y^+ is used to estimate the thickness of the first layer grid (Körpe et al., 2019):

$$y^+ = \frac{y\, u_\tau}{\nu} \tag{4}$$

where u_τ is friction velocity, y is the distance of the first layer grid from the boundary wall, ν is motion viscosity. Simulation results show that $y^+ < 1$ can be satisfied for the first layer grid.

According to (White, 1979), the thickness of the first layer grid can be estimated as:

$$\Delta_s = \frac{y^+ \mu}{U_{fric} \cdot \rho} \tag{5}$$

where Δ_s is the mesh thickness of the first layer near the bridge section, ρ is the freestream density, μ is dynamic viscosity, and U_{fric} is friction velocity. According to the formula, the thicknesses of the first layer grid are $3.3\times10^{-4}B$ and $3.4\times10^{-4}B$ for sections A and B, respectively. Based on the data obtained by back-calculating from the Courant number (eq. 6), using a uniform time step of 0.0001s, the transition period is approximately 8s before reaching a stable phase. The average time period after stabilization is around 0.2s.

$$Co = \frac{u\Delta t}{\Delta x} \tag{6}$$

where u represents the fluid velocity, Δt represents the time step, and Δx represents the grid size.

We employed wall functions in our simulations. Without using wall functions, the mesh needs to be fully resolved down to the viscous sublayer, which requires a y^+ value of less than 1 (Bruno et al., 2008). This high mesh resolution is a computationally expensive approach. Wall functions, however, allow us to avoid this computationally expensive approach. The key to using the wall function lies in its ability to simplify the flow calculation in the near-wall region through empirical formulas and semi-theoretical models, thus eliminating the need for fine grid independence verification near the wall. The wall function can reasonably handle the near-wall flow of high-Reynolds-number turbulence under coarser grid conditions, thereby reducing sensitivity to grid resolution. The first layer of the mesh can be placed directly within the logarithmic region, and the wall function will operate based on a predefined velocity profile until the specified y^+ value is reached. Fig. 4 shows a schematic diagram of the wall function. As a result, the influence of mesh size can be neglected. In OpenFOAM, wall functions operate under strict rules, which are as follows.

In the viscous sublayer region,

$$u^+ = y^+ \tag{7}$$

where u^+ represents the dimensionless velocity based on the friction velocity u_t.

In the logarithmic layer,

$$u^+ = \frac{1}{\kappa}\ln(Ey^+) \tag{8}$$

where $\kappa = 0.41$, and $E = 9.8$

In the buffer layer, the transition between calculations in the viscous sublayer and the logarithmic layer is determined based on the value of y^+.

The wall function simplifies the handling of near-wall flow, reducing the need for grid refinement and thereby alleviating the pressure imposed by Courant number limitations. However, even with the use of the wall function, controlling the Courant number remains crucial for ensuring numerical stability. This is especially important in explicit time integration methods, where

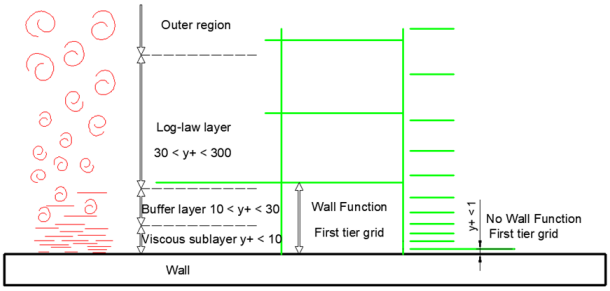

Fig. 4 Working sketch of wall function

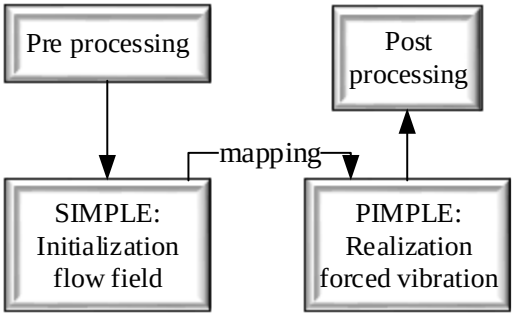

Fig. 5 Implementation of forced vibration process using OpenFOAM

adjusting the time step or grid resolution is necessary to keep the Courant number within a reasonable range (Brusiani et al., 2013).

The open-source code OpenFOAM was used to perform the forced vibration simulations. Solving N-S equations and updating dynamic grids are the two key points during the implementation of the forced vibration process. As shown in Fig. 5, after the preprocessing, the steady-state SIMPLE algorithm is first used to initialize the flow field, and the results are mapped to the computational domain. Then, the transient PIMPLE algorithm is used to solve the flow field with a time step length of 0.0001 s. The aeroelastic forces on the bridge deck are recorded at each time step, which are used to calculate flutter derivatives.

3. NUMERICAL SIMULATION

3.1 Effect of Turbulence Models

To evaluate the effect of turbulent models, the SST k-ω and k-ε models (Jiang et al., 2018) are used and studied in this paper. The other initial calculation conditions are set as 0° wind attack angle, the dimensionless amplitude h/B = 0.01 – 0.035 for vertical bending motion, and torsional amplitude = 1° – 10° for torsional motion. Based on this engineering range (Wang et al., 2014), we selected h/B = 0.02 and a torsional amplitude of 2°. The Reynolds numbers for sections A and B may exceed 2.1×10^7 under actual conditions. In this study, a 10:1 model scaling was applied. Considering the reduced wind speed range of 2 to 14, we selected Re = 6.2×10^6 and 6.0×10^6, which correspond well with the actual operating conditions. The flutter derivatives for sections A and B are plotted against the reduced wind speed $2\pi U/(B\omega)$ in Figs. 6 and 7, respectively.

For section A (Fig. 6), compared with the k-ε model, A_1^* values from the SST k-ω model are close to the experimental values of Poulsen et al. (1992) at low reduced wind speed at least. The A_2^* and A_3^* from the two turbulence models are comparable. When the Root Mean Square Error (RMSE) between two sets of results is less than 0.5, two sets of results are considered close. Their values agree well with the experimental results at low reduced wind speeds while the deviations between the numerical and experimental results become larger at higher reduced wind speeds. The values from the two turbulence models are close to the experimental results at low reduced wind speeds, with RMSE values below 0.2 (Table 1). The H_1^* and H_2^* from the two turbulent models are close to the experimental results at low reduced wind speeds; however, with increasing reduced wind speed, the results from the k-ε model deviate from the experimental ones, especially for H_2^*. Obviously, the results of the SST k-ω model are more reliable than those of the k-ε model. For H_3^*, when the reduced wind speed is less than 8, the results of the SST k-ω model are closer to the experimental values than those of the k-ε model. The H_4^* errors of the two models are relatively large, reflecting the influence of vertical displacement on lift force. The RMSE for the SST k-ω model reached 0.5911(Table 1). This derivative is highly sensitive to wind speed and vortex shedding, which can lead to significant discrepancies between the numerical simulations and experimental results. However, the overall trend remains consistent.

For section B (Fig. 7), the estimates of A_1^*, A_2^*, A_3^*, H_2^*, H_3^* using k-ε model are closer to the experimental results than those using SST k-ω model. The RMSE in Table 2 demonstrates that the errors of the k-ε model are consistently smaller than those of the SST k-ω model. The values of H_1^* from k-ε model are closer to the experimental values for the reduced wind speed of less than 4. With the increase of reduced wind speed, the results from the two turbulent models both deviate from the experiments. Since $H_2^*, H_4^*, A_2^*, A_4^*$ are cross-flutter derivatives, they tend to be more significantly influenced when slight disturbances occur in the direct flutter derivatives under higher wind speeds. In experiments, the disturbances generated by the bridge are larger compared to those seen in numerical simulations. This discrepancy can be attributed to the fact that real-world structures are

Table 1 Root-mean-square error at low wind speeds ($2\pi U/B\omega \leq 8$) for section A

	A_1^*	A_2^*	A_3^*	A_4^*	H_1^*	H_2^*	H_3^*	H_4^*
SST	0.00246	0.112	0.00655	0.01865	0.0212	0.158	0.0526	0.5911
k- ε	0.0223	0.125	0.0074	0.0511	0.0305	0.09102	0.3408	0.4499

Table 2 Root mean square error at low wind speeds (2πU/Bω≤6) for section B

	A_1^*	A_2^*	A_3^*	A_4^*	H_1^*	H_2^*	H_3^*	H_4^*
SST	0.0188	0.1204	0.0374	0.0669	0.4337	0.4195	0.3861	0.4721
k-ε	0.0191	0.0112	0.1148	0.0062	0.4538	0.0455	0.0069	0.5884

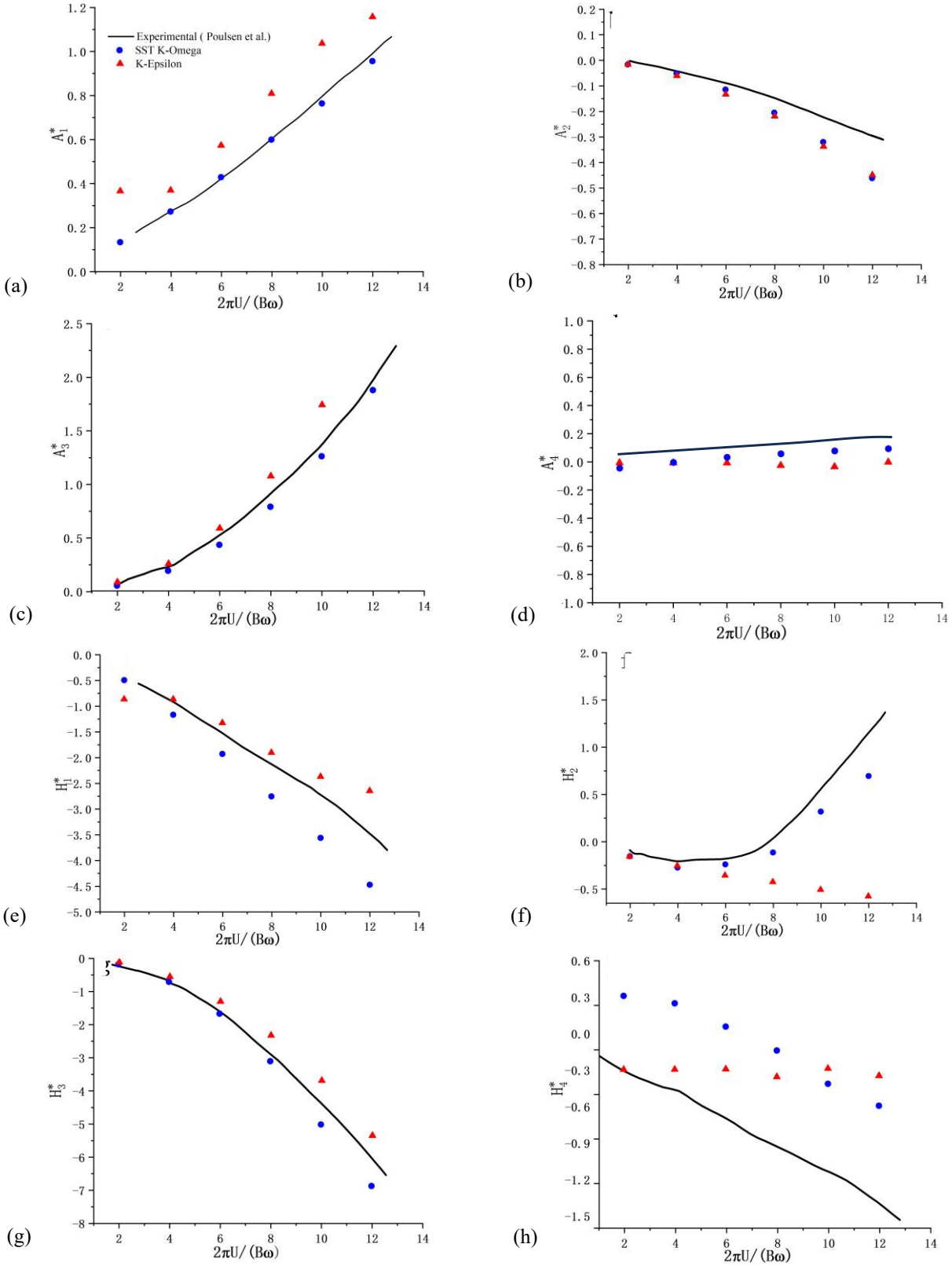

Fig. 6 Comparison of flutter derivatives for section A obtained from different turbulence models with those obtained experimentally by Poulsen et al. (1992)

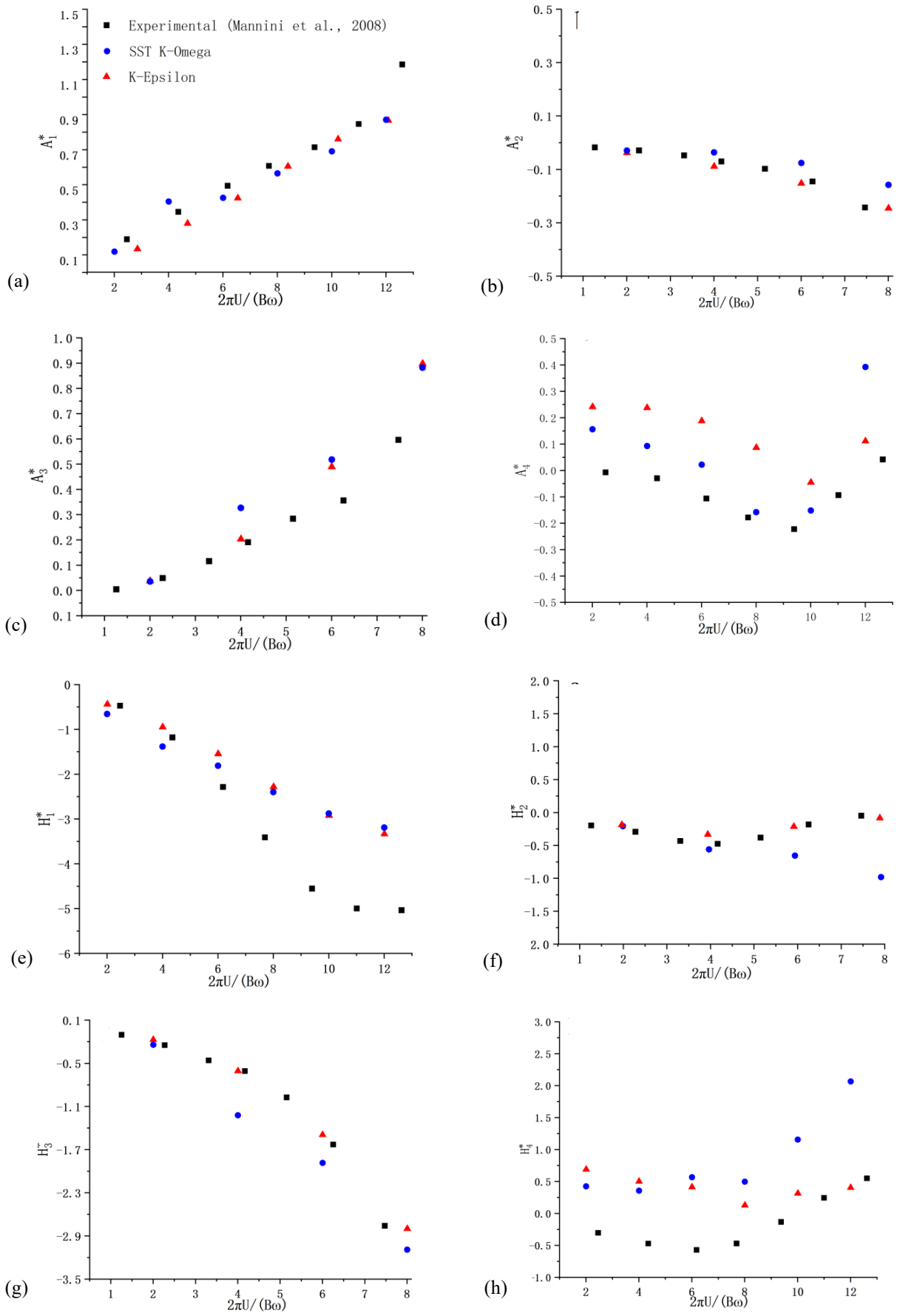

Fig. 7 Comparison of flutter derivatives for section B obtained from different turbulence models with those obtained experimentally by Mannini and Bartoli (2008)

Table 3. Identification of flutter derivatives under different Reynolds numbers

Section	Re	A_1^*	A_2^*	A_3^*	A_4^*	H_1^*	H_2^*	H_3^*	H_4^*
A	6.2×10^4	0.428	0.110	0.436	0.031	1.617	0.254	1.659	0.061
	6.2×10^5	0.429	0.110	0.436	0.033	1.620	0.249	1.661	0.064
	6.2×10^6	0.429	0.111	0.436	0.034	1.621	0.240	1.662	0.063
	6.2×10^7	0.429	0.110	0.436	0.034	1.622	0.241	1.659	0.062
B	6.0×10^4	0.416	-0.142	0.424	-0.045	-1.508	-0.184	-1.476	0.410
	6.0×10^5	0.423	-0.150	0.431	-0.031	-1.530	-0.214	-1.485	0.428
	6.0×10^6	0.424	-0.151	0.432	-0.026	-1.539	-0.231	-1.488	0.418
	6.0×10^7	0.424	-0.151	0.433	-0.027	-1.544	-0.203	-1.497	0.411

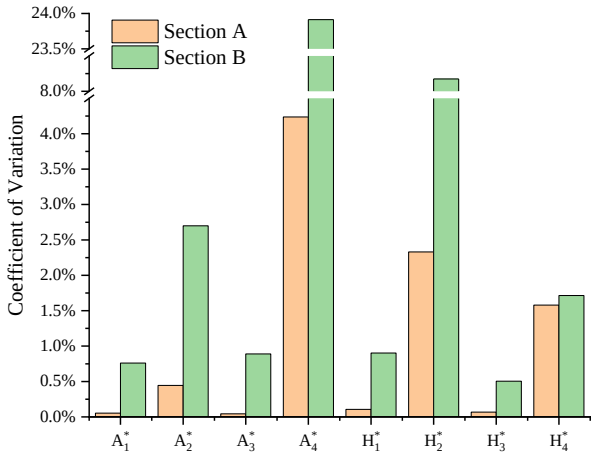

Fig. 8 Variations of flutter derivative coefficient with Reynolds number

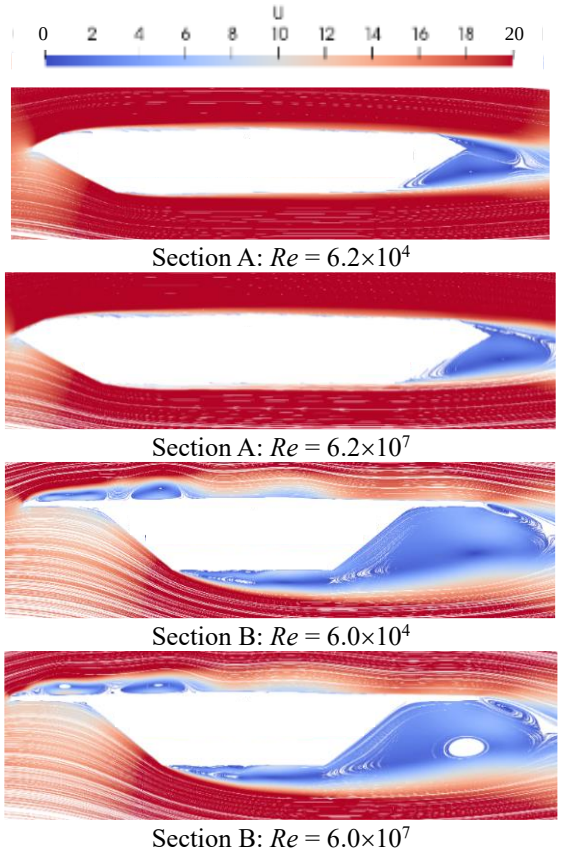

Fig. 9 Streamline traces around the bridge decks A and B at different Reynolds numbers

exposed to more complex wind conditions, including turbulence, variability in wind direction, and other environmental factors, which are difficult to fully replicate in simulations.

According to Matsumoto et al. (1999), A_1^*, A_2^* and H_3^* are the key parameters that dominate the flutter performance of a bridge deck. Therefore, it might be concluded from the above analyses that the SST k-ω model is more suitable for section A while the k-ε model is more suitable for section B in view of flutter derivatives identification by forced vibration method.

3.2 Effect of Reynolds Number

To evaluate the effect of Reynolds numbers on flutter derivative identifications, a range of Reynolds numbers (6.0×10^4 - 6.2×10^7) are considered. The other initial conditions are the reduced wind speed of 6, the wind attack angle of 0°, the dimensionless vertical bending amplitude of 0.02, and the torsion amplitude of 2°. The identification results of flutter derivatives under different Reynolds numbers are shown in Table 3, and the coefficients of variation (i.e., the ratio of the standard deviation to the mean value) of sections A and B are drawn in Fig. 8. For both sections, the variation of A_4^* is significant. However, the effect of A_4^* on the flutter performance of a bridge deck is very weak, and hence the variation of A_4^* is uninterested. Without considering A_4^*, for section A, H_2^* has the largest variation coefficient of 2.3%, followed by 1.5% of H_4^*. The variation coefficients of other flutter derivatives are all lower than 0.5%.

For Section B, H_2^* has the largest coefficient variation of 8.1%, followed by 2.6% of A_2^* and 1.7% of H_4^*. The variation coefficients of other flutter derivatives are lower than 1%. It can be concluded that the influence of the Reynolds number on flutter derivatives is much greater for section B than for section A.

Figure 9 shows the streamline traces for sections A and B at Re = 6.0×10^4 and 6.2×10^7. For section A, flow remains attached on its surface, and the flow features are

similar for the two Reynolds numbers. Therefore, the coefficient of variation for the flutter derivatives is smaller, and no significant vortex formation is observed in the wake of the bridge section. This indicates that the risk of flutter and aerodynamic instability of the bridge is relatively low. For section B, the flow separates from the leading corner of the deck, spawning vortices on the upper surface.

The vortices grow in size when the Reynolds number is increased. The increase in vortex size implies a higher likelihood of generating larger vortices and recirculation zones, which can lead to stronger fluid-structure interactions. This can result in significant changes in the flutter derivatives associated with torsional motion, yielding a strong fluid-structure coupling. The flow feature on the rear side also differs between the two Reynolds numbers. It can thus be said that the effect of the Reynolds number on flutter derivatives is much larger for section B than for section A.

3.3 Effect of Motion Amplitude

It is often assumed that the self-excited forces are linear functions of the state vector of the bridge deck, as presented in Eq. (2). The assumption is valid for cases of small disturbance, i.e., small vibration amplitude. However, for the cases of large amplitude vibrations, the self-excited forces display nonlinear features. To evaluate the effects of vibration amplitudes on flutter derivatives, numerical simulations were carried out for several vibration amplitudes. For vertical motions, the dimensionless amplitude h/B is within 0.01~0.035. For torsional motions, the amplitude varies from 1° to 10°. The other adopted setting conditions are: the dimensionless wind speed is 6, the wind attack angle is 0°, and Re = 6.2×10^6 and 6.0×10^6 for sections A and B, respectively. The results for sections A and B are presented in Fig. 10.

As shown in Figs. 10(a-d), A_1^*, H_1^* and H_4^* are quite stable for the vertical amplitude range of 0.015~0.025, while showing obvious fluctuations when the vertical amplitude is greater than 0.025. The A_4^* varies irregularly with increasing vibration amplitude due to low ratios of the relevant force components. Fortunately, the identification error of A_4^* does not significantly affect the flutter analysis of a bridge deck.

As shown in Fig. 10 (e-h), for section A, A_2^* shows a gradual increasing trend with increasing torsional amplitude. The H_2^* and A_3^* do not change significantly when the amplitude is less than 4°, but increase sharply when the amplitude reaches 6°. The variation of H_3^* with increasing the vibration amplitude is small. For section B, when the amplitude is greater than 2°, the A_2^* starts to increase significantly. The variations of other flutter derivatives with increasing the vibration amplitude are very small. Overall, flutter derivative values can be considered constants if the vertical and torsional amplitudes are lower than 0.025 and 2°, respectively. Further increasing the vibration amplitude may result in remarkable variations of some flutter derivatives (e.g., A_1^* and A_2^*).

Figure 11 shows the fast Fourier transform spectrum of lift coefficient time histories for various vibration amplitudes. For section A (Fig. 11a), there are no obvious higher harmonics for the vertical bending amplitudes examined. However, a secondary peak occurs at the natural vortex shedding frequency marked by Strouhal number, which is gradually mitigated with increasing vibration amplitude. With the increase of torsional amplitude, obvious super-harmonics appear in the self-excited forces, which is a clear nonlinear feature of the self-excited force. As shown in Fig. 11a, the amplitude peaks at a frequency of 0.999 Hz for all cases (0.010 – 0.035), although the peak value declines with increasing amplitude, dropping from 0.11 at an amplitude of 0.035 to 0.032 at an amplitude of 0.010. This suggests that larger vertical vibration amplitudes enhance the aerodynamic response of the structure, but the peak value tends to stabilize at higher amplitudes. In the frequency range above 2 Hz, amplitude variations have minimal impact on the spectrum, with almost no significant fluctuations or secondary peaks in the high-frequency region, indicating that high frequencies have a limited effect on the aerodynamic response.

The primary low-frequency peak, located around 1.14 Hz (Fig. 11b), is also evident in the torsional vibrations. As the torsional angle increases from 1° to 10°, the amplitude at the frequency rises significantly, reaching approximately 0.43 at 10°, This indicates a strong correlation between the torsional angle and the intensity of the aerodynamic response. Secondary frequency peaks are observed at 3.28 Hz, 5.42 Hz, 7.42 Hz, and 8.57 Hz. Although these secondary frequencies exhibit much lower amplitudes than the primary frequency, they demonstrate that increasing torsional results in a more complex aerodynamic response, with the emergence of multiple harmonic components. The amplitude of these secondary peaks increases with increasing torsional angles, peaking at 3.28 Hz with a value of about 0.034 before gradually decreasing at higher frequencies. The effect of torsional angle is evident not only in the significant increase of the primary peak but also in the more pronounced secondary peaks, suggesting that larger torsional angles lead to more complex aerodynamic behavior and nonlinear phenomena.

For section B (Fig. 11c, d), no obvious peak at the vortex shedding frequency is observed under different vertical bending amplitudes while obvious super-harmonic peaks appear with the increase of torsional amplitude. In the vertical bending vibration of Section B, the primary frequency peak consistently appears around 0.71 Hz. As the amplitude increases from 0.010 to 0.035, the amplitude at this primary frequency gradually rises from 0.032 at an amplitude of 0.010 to 0.11 at an amplitude of 0.035. This trend indicates that larger vertical amplitudes enhance the aerodynamic response of the structure; however, at higher amplitudes, this enhancement tends to stabilize, leading to a diminishing impact on aerodynamic characteristics. In the high-frequency region (above 2 Hz), almost no noticeable secondary peaks are discernible, suggesting that higher frequencies have minimal effect on the aerodynamic response.

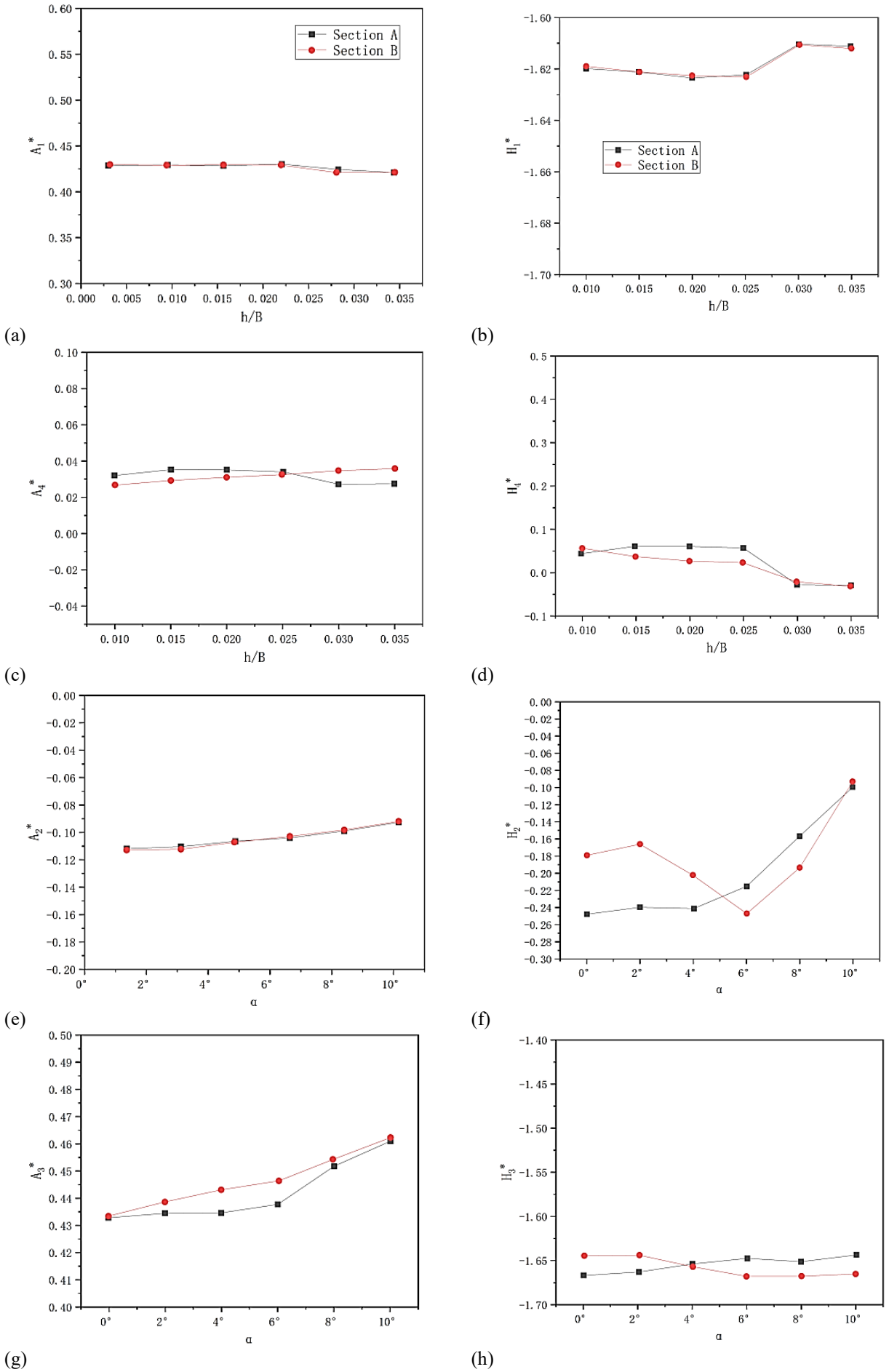

Fig. 10 Dependence of flutter derivatives on oscillation amplitudes

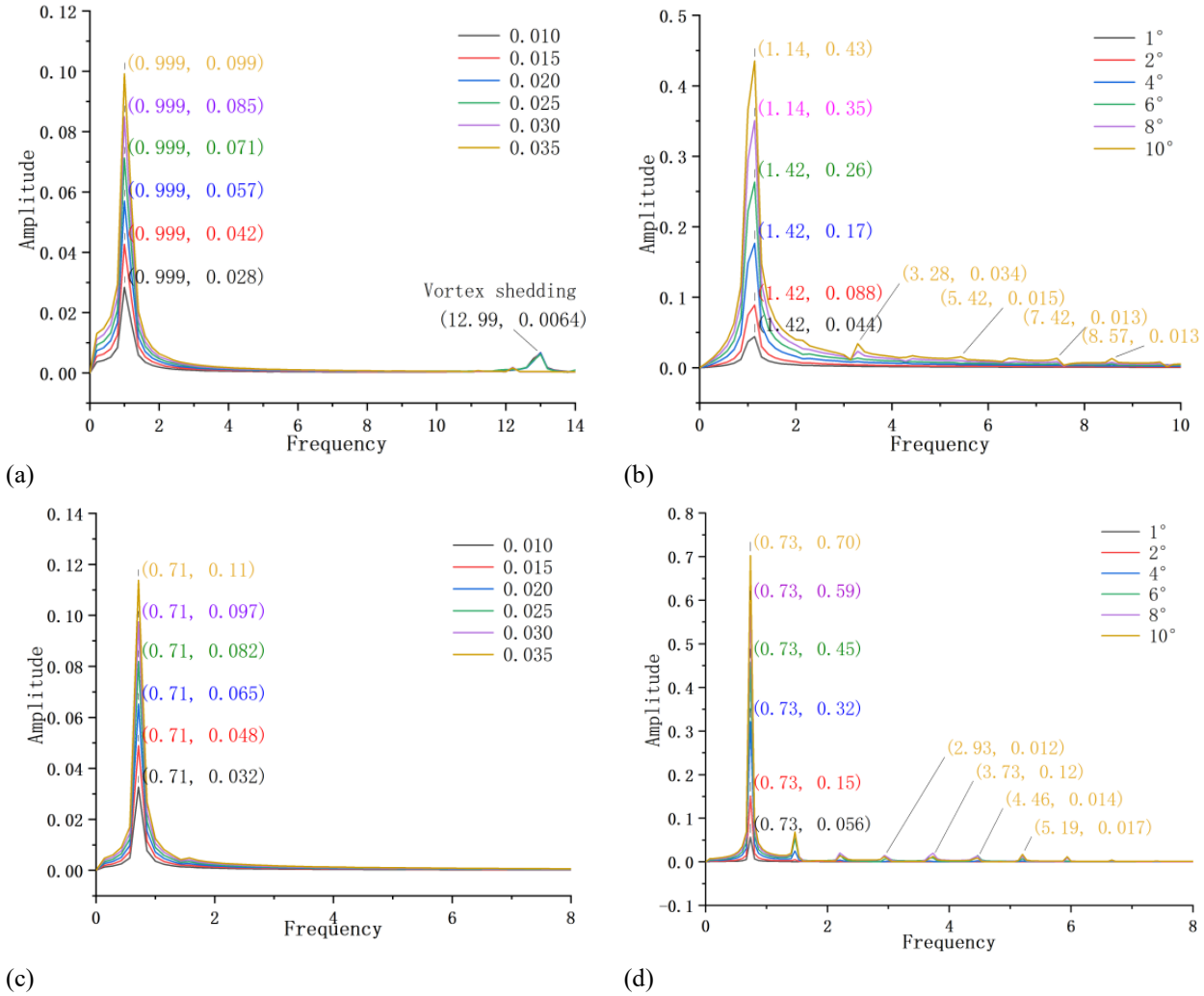

Fig. 11 Power spectra of lift coefficient time histories under different amplitudes: (a) vertical bending vibration of section A, (b) torsional vibration of section A, (c) vertical bending vibration of section B, and (d) torsional vibration of section B

In the case of the torsional vibration, the primary frequency peak consistently appears at 0.73 Hz and increases significantly as the torsional angle rises from 1° to 10°. The amplitude rises from 0.056 at 1° to 0.70 at 10°, indicating a substantial increase in aerodynamic response with increasing torsional angles. Multiple secondary peaks appear at higher frequencies, including 2.93 Hz, 3.73 Hz, 4.46 Hz, and 5.19 Hz. While the amplitudes of these secondary peaks are small, they increase gradually with increasing torsional angles, demonstrating that the structure's nonlinear response becomes more complex under greater torsional vibration. Especially at larger torsional angles, the aerodynamic coupling effect reveals more complex harmonic behaviors.

3.4 Effect of Attack Angles

According to the research results of Zhao et al. (2021), the angle of attack can be over 3° in mountainous areas of uneven terrain and can be as high as 7° under the action of a typhoon. Therefore, to evaluate the effect of attack angles on flutter derivatives identifications, attack angles of 0° ~ 10° are considered. As shown in Fig. 12, the horizontal line defines a zero angle of attack, and the attack angle is negative or positive when wind flows

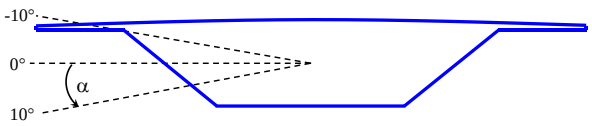

Fig. 12 Schematic diagram of wind attack angle

below or above the line. The other calculation conditions are: the dimensionless wind speed is 6, the vertical bending dimensionless amplitude is 0.02, and the torsion amplitude is 2°. The Reynolds numbers are $Re = 6.2\times10^6$ and 6.0×10^6 for sections A and B, respectively.

The estimated results are shown in Fig. 13. For section A (Fig. 13a, b), the values of A_2^* and H_4^* fluctuate irregularly, but the other derivatives vary almost linearly with the wind attack angle. It should be noted that variations of A_1^*, A_4^* and H_3^* are very small, lying in the range of 0°~±2°. On the other hand, as shown in Fig. 13(c, d), the effects of the attack angle on the flutter derivatives are more significant for section B than for section A. The significant variations in flutter derivatives can be attributed to small changes in the attack angle. This is because the pressure distribution on the bridge deck surface

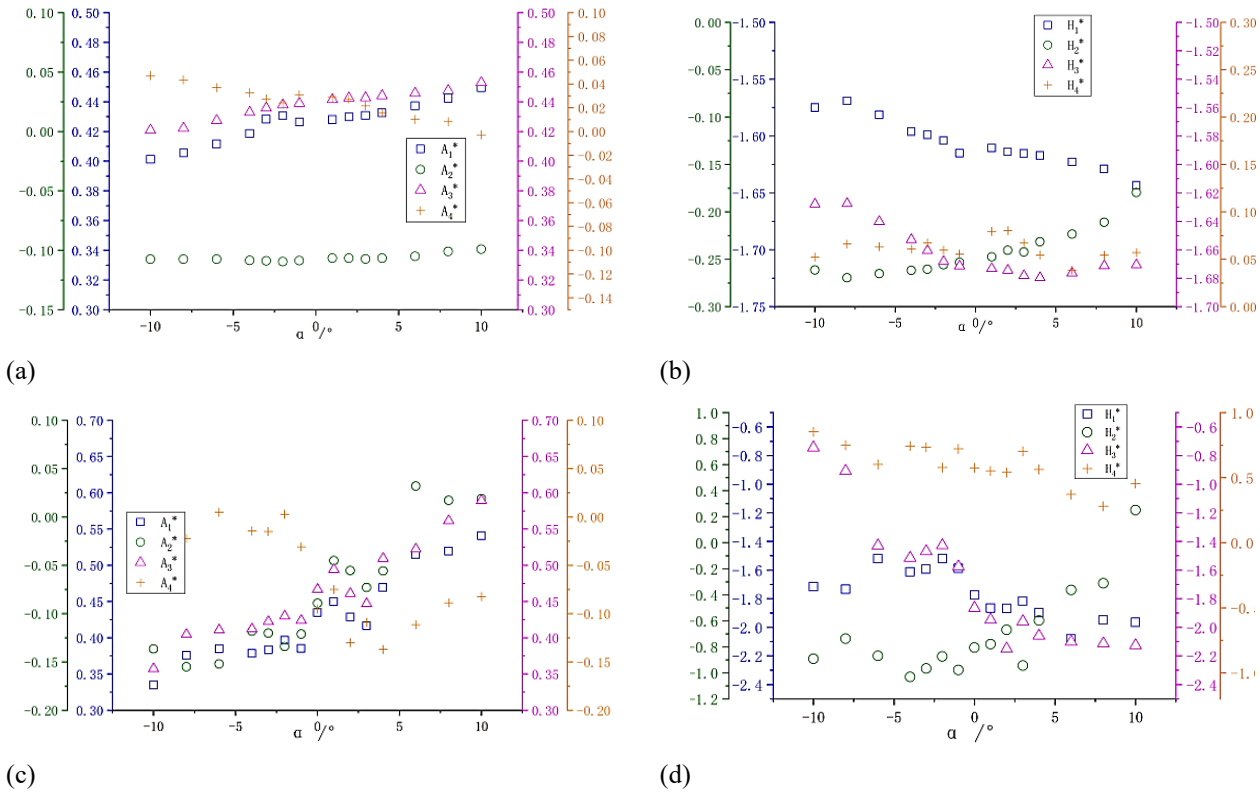

Fig. 13 Variations of flutter derivatives with attack angle: (a, b) section A, and (c, d) section B

changes with the attack angle, which in turn affects the overall self-excited forces and thus the flutter derivatives. Obviously, the effect of the attack angle on the self-excited forces of a bluff section is greater than that of a streamlined section.

4. CONCLUSIONS

In this paper numerical simulations of self-excited forces on streamlined and bluff bridge decks are performed using the open-source code OpenFOAM. The effects of turbulence model, Reynolds number, vibration amplitude and wind attack angle on the flutter derivative identifications are studied. The main conclusions are as follows.

(1) SST k-ω shows advantages in identifying flutter derivatives of a streamlined cross-section, while the k-ε model is suitable for the simulations of a bluff body section.

(2) When the Reynolds number ranges from 6.0×10^4 to 6.2×10^7, the average variations of flutter derivatives are less than 1.1% and 4.9% for sections A and B, respectively. The flutter derivatives of a bluff bridge deck are more sensitive to the Reynolds number. To accurately predict the critical wind speed for flutter instability, the effect of the Reynolds number should be considered, especially for bluff bridge decks.

(3) Flutter derivatives of the tested bridge decks can be considered constants if the vertical and torsional amplitudes are lower than 0.025 and 2°, respectively. Further increasing vibration amplitude may result in remarkable variations of some flutter derivatives. High-order harmonics exist in the self-excited forces for the cases with large amplitude vibrations, especially for the bluff bridge deck.

(4) Generally, the flutter derivatives are more sensitive to wind attack angle for section B than for section A. In the flutter analysis of a bridge, it is necessary to cover the possible range of wind attack angles, especially for the bluff bridge decks in areas with complex topography.

ACKNOWLEDGMENTS

The research in this paper was supported by three foundations: (*i*) National Natural Science Foundation of China (U23A20661); (*ii*) Special guiding fund for building energy conservation and green building in Zhenjiang City (zk20220001; JSU10SK2024ZX003).

CONFLICT OF INTEREST

The authors declare no conflict of interest.

AUTHORS CONTRIBUTION

Bo Su: Conceptualization, Methodology, Formal analysis, Writing original draft, Writing Review & Editing; **Yiwen Liu:** Formal analysis, Visualization, Writing original draft, Writing Review & Editing; **Mwansa Chambalile**: Writing review & editing ,Investigation Validation; **Gang Wang**:Writing Review & Editing Investigation Validation; **Md. Mahbub Alam**: Writing of the Final

Manuscript, Review & Editing, Visualization; **Ebarhim Barati**: Supervision, Methodology, Review & Editing.

REFERENCES

Abbas, T., Kavrakov, I., & Morgenthal, G. (2017). Methods for flutter stability analysis of long-span bridges: a review. *Proceedings of the Institution of Civil Engineers-Bridge Engineering*, 271-310. Thomas Telford Ltd. https://doi.org/10.1680/jbren.15.00039

Alam, M. M. (2023). Fluctuating forces on bluff bodies and their relationships with flow structures. *Ocean Engineering*, *273*, 113870. https://doi.org/10.1016/j.oceaneng.2023.113870

Amman, O. H., Karman, T., & Woodruff, G. B. (1941). The failure of the tacoma narrows bridge. https://doi.org/10.1201/9780367815646-13

Baetke, F., Warner. H., & Wengle, H. (1990). Numerical simulation of turbulent flow over surface-mounted obstacles with sharp edges and corners. *Journal of Wind Engineering and Industrial Aerodynamics*, *35*, 129-47. https://doi.org/10.1016/0167-6105(90)90193-g

Bhatt, R., & Alam, M. M. (2018). Vibration of a square cylinder submerged in a wake. *Journal of Fluid Mechanics, 853* ,301-332. https://doi.org/10.1017/jfm.2018.573

Bombardieri, R., Cavallaro, R., Sáez de Teresa, J. L., & Karpel, M. (2019). *Nonlinear aeroelasticity: a cfd-based adaptive methodology for flutter prediction*. AIAA Scitech 2019 Forum (p. 1866). https://doi.org/10.2514/6.2019-1866

Brownjohn, J. M. W., & Bogunovic, J. (2001). Strategies for aeroelastic parameter identification from bridge deck free vibration data. *Journal of Wind Engineering and Industrial Aerodynamics*, *89*, 1113-36. https://doi.org/10.1016/s0167-6105(01)00091-5

Bruno, L., & Fransos, D. (2008). Evaluation of reynolds number effects on flutter derivatives of a flat plate by means of a computational approach. *Journal of Fluids and Structures*, *24*, 1058-76. https://doi.org/10.1016/j.jfluidstructs.2008.03.001

Bruno, L., Khris, S, & Marcillat, J. (2001). Numerical simulation of the effect of section details and partial streamlining on the aerodynamics of bridge decks. *Wind and Structures*, *4*, 315-32. https://doi.org/10.12989/was.2001.4.4.315

Brusiani, F., Miranda, S. D., Patruno, L., Ubertini, F., & Vaona, P. (2013). On the evaluation of bridge deck flutter derivatives using RANS turbulence models. *Journal of Wind Engineering Industrial Aerodynamics*, *119*, 39-47. https://doi.org/10.1016/j.jweia.2013.05.002

Cao, B., & Sarkar, P. (2010, May, 23-27). *Identification of rational functions by forced vibration method for time-domain analysis of flexible structures.* Proceedings: The Fifth International Symposium on Computational Wind Engineering, Chapel Hill. https://doi.org/10.1016/j.engstruct.2012.05.003

Davenport, & Allan, G. (1962). Buffeting of a suspension bridge by storm winds. *Journal of the Structural Division*, *88*, 233–70. https://doi.org/10.1061/jsdeag.0000773

De Miranda, S., Patruno, L., Ricci, M., & Ubertini, F. (2015). Numerical study of a twin box bridge deck with increasing gap ratio by using RANS and LES approaches. *Engineering Structures*, *99*, 546-58. https://doi.org/10.1016/j.engstruct.2015.05.017

Jiang, L., Mingjun, D., Haomiao, S., & Yu, R. (2018). Numerical Modeling of flow over a rectangular broad-crested weir with a sloped upstream face. *Water*, *10*, 1663. https://doi.org/10.3390/w10111663

Körpe, D. S., Kanat, Ö. Ö., & Oktay, T. (2019). The Effects of initial y plus: numerical analysis of 3D NACA 4412 wing using γ-Reθ SST Turbulence model. *Avrupa Bilim ve Teknoloji Dergisi*, 692-702. https://doi.org/10.31590/ejosat.631135

Lin, C., & Alam, M. M. (2024). Intrinsic features of flow-induced stability of square cylinder. *Journal of Fluid Mechanics*, *988*, A50. https://doi.org/10.1017/jfm.2024.445

Lin, S., Qi, W., Nikolaos, N., & Haili, L. (2019). Effects of oscillation amplitude on motion-induced forces for 5: 1 rectangular cylinders. *Journal of Wind Engineering and Industrial Aerodynamics*, *186*, 68–83. https://doi.org/10.1016/j.jweia.2019.01.002

Mannini, C., & Bartoli, G. (2008). *Investigation on the dependence of bridge deck flutter derivatives on steady angle of attack.* Proc., BBAA VI Int. Colloquium on Bluff Bodies Aerodynamics and Applications. Citeseer. https://api.semanticscholar.org/CorpusID:221712605

Mannini, C., Sbragi, G., & Schewe, G. (2016). Analysis of self-excited forces for a box-girder bridge deck through unsteady RANS simulations. *Journal of Fluids and Structures*, *63*, 57-76. https://doi.org/10.1016/j.jfluidstructs.2016.02.007

Mondal, M., & Alam, M. M. (2023). Blockage effect on wakes of various bluff bodies: a review of confined flow. *Ocean Engineering,* 268, 115592. https://doi.org/10.1016/j.oceaneng.2023.115592

Matsumoto, M., Yoshizumi, F., Yabutani, T., Abe, K., & Nakajima, N. (1999). Flutter stabilization and heaving-branch flutter. *Journal of Wind Engineering and Industrial Aerodynamics, 83*, 289-99. https://doi.org/10.1016/s0167-6105(99)00079-3

Montoya, M. C., Nieto, F., Hernández, F., Kusano, I., Álvarez, A. J. & Jurado, J. Á. (2018). CFD-based aeroelastic characterization of streamlined bridge deck cross-sections subject to shape modifications using surrogate models. *Journal of Wind Engineering and Industrial Aerodynamics*, *177*, 405-28. https://doi.org/10.1016/j.jweia.2018.01.014

Neuhaus, C., Höffer, R., & Roesler, S. (2009). *Identification of 18 Flutter derivatives by forced vibration tests: A New experimental rig*. Identification of 18 Flutter Derivatives by Forced Vibration Tests, 1000-04. https://api.semanticscholar.org/CorpusID:124841633

Noda, M., Utsunomiya, H., Nagao, F., Kanda, M., & Shiraishi, N. (2003). Effects of oscillation amplitude on aerodynamic derivatives. *Journal of Wind Engineering Industrial Aerodynamics*, *91*, 101-11. https://doi.org/10.1016/s0167-6105(02)00338-0

Patruno, L. (2015). Accuracy of numerically evaluated flutter derivatives of bridge deck sections using RANS: Effects on the flutter onset velocity. *Engineering Structures*, *89*, 49-65. https://doi.org/10.1016/j.engstruct.2015.01.034

Poulsen, N. K., Damsgaard, A., & Reinhold, T. A. (1992). Determination of flutter derivatives for the Great Belt Bridge. *Journal of Wind Engineering and Industrial Aerodynamics*, *41*, 153–64. https://doi.org/10.1016/0167-6105(92)90403-w

Ribes, A., & Caremoli, C. (2007). S*alome platform component model for numerical simulation.* International Computer Software & Applications Conference. https://doi.org/10.1109/compsac.2007.185

Scanlan, R. H., & Tomo, J. (1971). Air foil and bridge deck flutter derivatives. *Journal of Soil Mechanics & Foundations Div*. https://doi.org/10.1061/jmcea3.0001526

Scanlan, R. H. (1993). Problematics in formulation of wind-force models for bridge decks. *Journal of Engineering Mechanics*, *119*, 1353–75. https://doi.org/10.1061/(asce)0733-9399(1993)119:7(1353)

Schewe, G., & Larsen, A. (1998). Reynolds number effects in the flow around a bluff bridge deck cross section. *Journal of Wind Engineering Industrial Aerodynamics*, *74*, 829-38. https://doi.org/10.1016/s0167-6105(98)00075-0

Siedziako, B., Øiseth, O., & Rønnquist, A. (2017). An enhanced forced vibration rig for wind tunnel testing of bridge deck section models in arbitrary motion. *Journal of Wind Engineering and Industrial Aerodynamics*, *164*, 152-63. https://doi.org/10.1016/j.jweia.2017.02.011

Starossek, U., Aslan, H., & Thiesemann, L. (2009). Experimental and numerical identification of flutter derivatives for nine bridge deck sections. *Wind and Structures*, *12*, 519. https://doi.org/10.12989/was.2009.12.6.519

Tang, H., Li, Y., & Shum, K. M. (2018). Flutter performance of long-span suspension bridges under non-uniform inflow. *Advances in structural Engineering*, *21*, 201-13. https://doi.org/10.1177/1369433217713926

Tang, H., Shum, K. M., & Li, Y. (2019). Investigation of flutter performance of a twin-box bridge girder at large angles of attack. *Journal of Wind Engineering Industrial Aerodynamics*, *186*, 192-203. https://doi.org/10.1016/j.jweia.2019.01.010

Wang, L., Liu, Z., & Chen, Z. (2014). Multi-state and multi-frequency forced vibration identification of flutter derivatives of bridge sections. *Vibration and Shock,* *37*, 20-28. https://link.cnki.net/doi/10.13465/j.cnki.jvs.2018.20.003

White, F. M. (1979). *Fluid mechanics* (Tata McGraw-Hill Education). https://doi.org/10.1007/3-540-27223-2_1

Wu, B., Wang, Q., Liao, H., Li, Y., & Li, M. (2020). Flutter derivatives of a flat plate section and analysis of flutter instability at various wind angles of attack. *Journal of Wind Engineering and Industrial Aerodynamics*, *196*, 104046. https://doi.org/10.1016/j.jweia.2019.104046

Xu, F., Ying, X., & Zhang, Z. (2016). Effects of exponentially modified sinusoidal oscillation and amplitude on bridge deck flutter derivatives. *Journal of Bridge Engineering*, *21*, 06016001. https://doi.org/10.1061/(asce)be.1943-5592.0000884

Xu, F., & Zhang, Z. (2017). Free vibration numerical simulation technique for extracting flutter derivatives of bridge decks. *Journal of Wind Engineering and Industrial Aerodynamics*, *170*, 226–37. https://doi.org/10.1016/j.jweia.2017.08.018

Zhang, M., Xu, F., & Han, Y. (2020a). Assessment of wind-induced nonlinear post-critical performance of bridge decks. *Journal of Wind Engineering and Industrial Aerodynamics*, *203*, 104251. https://doi.org/10.1016/j.jweia.2020.104251

Zhang, M., Xu, F., Wu, T., & Zhang, Z. (2020b). Postflutter Analysis of bridge decks using aerodynamic-describing functions. *Journal of Bridge Engineering*, *25*, 04020046. https://doi.org/10.1061/(asce)be.1943-5592.0001587

Zhang, M., Xu, F., Zhang, Z., & Ying, X. (2019). Energy budget analysis and engineering modeling of post-flutter limit cycle oscillation of a bridge deck. *Journal of Wind Engineering and Industrial Aerodynamics*, *188*, 410-20. https://doi.org/10.1016/j.jweia.2019.03.010

Zhang, Z., & Zhang, W. (2017). Experimental investigation on relations between flutter derivatives and aerodynamic admittances. *Journal of Bridge Engineering*, *22*, 04017068. https://doi.org/10.1061/(asce)be.1943-5592.0001117

Zhao, L, Wu, F, & Pan, J. (2021). Wind field characteristics and wind-induced buffeting response of a long-span bridge during the landing of a strong typhoon Journal of Aerodynamics, 39 , 86-97. https://doi.org/10.7638/kqdlxxb-2021.0066

Zheng, Q., & Alam, M. M. (2017). Intrinsic features of flow past three square prisms in side-by-side arrangement. *Journal of Fluid Mechanics, 826*, 996 –

1033. https://doi.org/10.1017/jfm.2017.378

Zheng, Q., & Alam, M. M. (2019). Evolution of the wake of three inline square prisms. *Physical Review Fluids*, *4*(10), 104701. https://doi.org/10.1103/physrevfluids.4.104701

Zhou, Z., & Ma, R. (2010). Numerical simulation study of the Reynolds number effect on two bridge decks based on the deterministic vortex method. *Wind and Structures*, *13*, 347-62. https://doi.org/10.12989/was.2010.13.4.347

Zhou, Y., Hao, J., & Alam, M. M. (2024). Wake of two tandem square cylinders. *Journal of Fluid Mechanics*, *983*, A3. https://doi.org/10.1017/jfm.2024.119